ACS SENSORS

pubs.acs.org/acssensors

Article

Single-Entity Approach to Investigate Surface Charge Enhancement in Magnetoelectric Nanoparticles Induced by AC Magnetic Field Stimulation

Popular Pandey, Govinda Ghimire, Javier Garcia, Alberto Rubfiaro, Xuewen Wang, Asahi Tomitaka, Madhavan Nair, Ajeet Kaushik,* and Jin He*

Cite This: *ACS Sens.* 2021, 6, 340−347

Read Online

ACCESS | Metrics & More | Article Recommendations | Supporting Information

ABSTRACT: Magneto-electric nanoparticles (MENPs), composed of a piezoelectric shell and a ferromagnetic core, exhibited enhanced cell uptake and controlled drug release due to the enhanced localized electric field (surface charge/potential) and the generation of acoustics, respectively, upon applying alternating current (AC) magnetic (B)-field stimulation. This research, for the first time, implements an electrochemical single-entity approach to probe AC B-field induced strain mediated surface potential enhancement on MENP surface. The surface potential changes at the single-NP level can be probed by the open circuit potential changes of the floating carbon nanoelectrode (CNE) during the MENP-CNE collision events. The results confirmed that the AC B-field (60 Oe) stimulation caused localized surface potential enhancement of MENP. This observation is associated with the presence of a piezoelectric shell, whereas magnetic nanoparticles were found unaffected under identical stimulation.

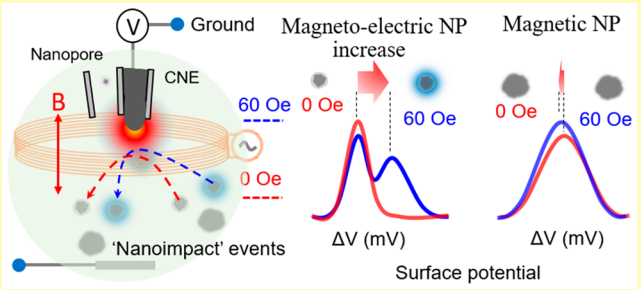

KEYWORDS: *Magneto-electric nanoparticles, surface charge probing, carbon nanoelectrode, nanoimpact, single-entity experiment, nanopipette*

Contribution of stimuli-responsive smart multifunctional nanosystems in biomedical science is emerging to enable investigation of novel theranostics of desired performance.[1] Most of these nanosystems need external stimulation to exhibit the desired performance. During the process of stimulation, these nanosystems showed altered intrinsic properties which may cause beneficial or adverse effects in biological systems. Among various stimuli-responsive nanosystems explored for biomedical applications, magnetoelectric nanoparticles (MENPs) are emerging as a multifunctional multiferroic nanosystem. The MENPs exhibited unique aspects suitable for biomedical science due to controllable coupling between magnetic and electronic properties.[2−4] This nanosystem is a core−shell nanostructure comprising a magnetostrictive core of cobalt ferrite ($Co_2Fe_2O_4$, i.e., CFO) and ferroelectric shell of barium titanate ($BaTiO_3$, i.e., BTO).[4−6] The MENP acts as a multifunctional material on application of alternating current (AC) magnetic field due to the presence of the magnetic core and piezoelectric shell.[2,4,7] Upon inducing the AC B-field, the MENP core went through the strain deformation which was further absorbed by the shell to produce a magneto-elastic wave.[4] The surface potential of MENPs is also altered to cause a change in polarization. Due to the controlled magneto-electric nature, in addition to biological applications, the MENP is also an ideal candidate for several other applications, some of which include magnetic-field sensors, miniature antennas, high-density data storage, spintronics, energy harvesters, and microelectromechanical systems where a magneto-electro-elastic coupling is an essential requirement.[8−12]

We have explored MENP as a potential biocompatible drug nanocarrier to deliver a targeted therapeutic agent across the blood-brain barrier.[5,13] On-demand release of bioactives (anti-HIV drug, siRNA, and edited gene Cas9/gRNA) from MENPs based nanomedicine on applying AC B-field stimulation have also been recently demonstrated.[14−16] The findings of these research suggests that the MENP based nanomedicine exhibited an enhanced therapeutic effect. The mechanism behind the rapid cell-uptake and on-demand drug release is likely related to the rotational motion, the magneto-elastic wave, and the generation of localized tunable/reversible surface charge change of MENPs under AC B-field stimulation. While

Special Issue: Commemorating NJ Tao

Received: April 1, 2020
Accepted: May 25, 2020
Published: May 25, 2020

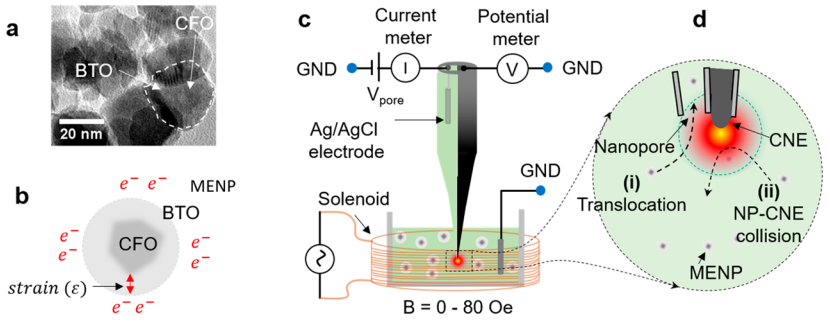

Figure 1. (a) TEM image of the MENP showing (CFO) core and (BTO) shell (dotted region). (b) Schematic illustration of the CFO-BTO MENPs' strain mediated localized surface charge enhancement in the presence of AC B-field. Strain (ε) denotes the directional strain generated at the CFO core. The redistribution of charge is indicated by the electrons. (c) Experimental setup for the detection of the surface potential of single NP by using the CNE nanopore nanopipette. V_{pore} is the applied bias. Potential (V) is measured by using a high impedance differential amplifier. The gradient red-colored region around the nanopipette apex represents the potential sensing zone of the nanoelectrode. MENPs are suspended in the bath solution. The yellow coil around the vial is a solenoid to apply AC B-field. (d) Zoomed image of the nanopipette apex in (a) (not to scale). The curved dashed arrows represent the nanopore translocation and MENP-CNE collision events under AC B-field stimulation.

theoretically formulated, an experimental demonstration of the mechanism, along with quantification of this scientific reasoning, has not been accomplished yet.

Ultrasensitive detection of surface properties is essential in the fields of surface science,[17] colloid science,[18−21] mineralogy,[22−24] and understanding of chemical/biological processes at the nanoparticle(NP)−biological system interfaces.[17,18,25−32] Methodologies such as zeta potential and potentiometric titration are in practice to estimate the average surface charge density change of a nanosystem suspended in solution.[33−35] Recently, single-entity electrochemistry techniques[36−39] are emerging as potential solutions that can effectively probe the physicochemical properties, including surface charge, of the single entities in the electrolyte. These single-entity approaches can also provide more fundamental and technological information than conventional ensemble methodologies.[37,38]

Here, we are demonstrating the detection of surface charge enhancement of individual MENPs under AC B-field through collision events of MENPs at the carbon nanoelectrode (CNE) of a nanopore−nanoelectrode nanopipette.[40,41] The collision events of individual NPs at the CNE are detected by an open-circuit potential (OCP) detection method, which has been validated using gold NPs and polystyrene NPs.[41] The AC B-field stimulation is generated by electromagnetic coils. The majority of the measurements were made at 60 Oe. The previous studies confirm the stimulation at this magnitude is optimized and safe, which causes effective cell uptake via nanoelectroporation[5] and release of therapeutic agents from the surface of MENPs-based nanoformulation.[14,15] Noticeable differences in the induced potential signal changes during MENP-CNE collision events were observed only in the case of AC B-field stimulation due to localized surface potential increment on the surface of MENP. In contrast, the surface potential enhancement was not observed in the absence of AC B-field stimulation or when magnetic nanoparticles (MNP) were used.

EXPERIMENTAL SECTION

Materials and Reagents. ACS grade chemicals (e.g., phosphate buffer saline (PBS) for pH 7.3−7.5) were purchased from Fisher Scientific and used without any further purification. The MENPs utilized in this research were synthesized and characterized using our established and published protocol.[5] Iron oxide nanoparticles (~50−100 nm) as magnetic nanoparticles (MNPs) were purchased from Sigma-Aldrich. Gold nanoparticles (GNP) of 40 nm were purchased from BBI Solutions Inc. The 3-cyanopropyldimethylchlorosilane for nanopipette surface modification was obtained from Fisher Scientific. Redox molecule hexaammineruthenium(III) chloride [Ru $(NH3)_6Cl_3$] (98% pure) was purchased from Sigma-Aldrich. All solutions were prepared using DI water (~18 MΩ) (Ultra Purelab System, ELGA/Siemens).

Salinization. The quartz surface of the nanopore−nanoelectrode nanopipette tip was chemically modified following the previously reported method.[42] In brief, the nanopipette tip (<5 mm) was immersed in a 2% (v/v) solution of 3-cyanopropyldimethylchlorosilane in acetonitrile (CH_3CN) for 2 h to ensure the surface modification of exterior of the nanopipette. The nanopipette was then rinsed sequentially with CH_3CN, EtOH, and DI water followed by argon gas drying. This modified nanopipette was characterized using electrochemical measurements and further used for the experiment.

Electrical and Electrochemical Measurements. The fabrication and characterization methods of the nanopore−CNE nanopipette have been reported in our previously published research.[43] In brief, the ionic current−time (i−t) and potential−time (V−t) traces are recorded using the experimental setup as illustrated in Figure 1a. The setup is housed in double Faraday cages on an air floating optical table to reduce electrical and mechanical noise. We used homemade Ag/AgCl electrodes and an Axopatch 200B amplifier (Molecular Devices Inc., CA) in voltage-clamp mode to measure the ionic current through the nanopore. A customized, battery-powered, high-input impedance differential amplifier was used to measure the OCP of the CNE. A digital oscilloscope (Yokogawa DL850 Scopecorder) was used to record the current and potential traces with a sampling rate of 50 kHz. The bandwidth of the low-pass filter was 5 kHz for current and 40 kHz for potential signals. All experiments and measurements were performed at room temperature. The collision experiments were performed in 10 mM PBS. The NP concentration in the bath solution was typically 1 nM if not mentioned otherwise.

AC B-Field Stimulation. To enhance the throughput of single-MENP measurements, we apply AC B-field via a custom-built solenoid. An AC voltage of 20 V peak-to-peak (V_{pp}) magnitude at 1 kHz frequency (f_{ac}) was applied to the CNE using a Function generator (Keithley 3390). The current in the solenoid was applied using a DC power supply (Keithley 2230-30-1). The current in the solenoid coil was varied to adjust B-field intensity at the center of the solenoid. The heat produced in the coil was negligible (temperature difference varies from 23 to 26 °C) for measurement ~15 min. However, to avoid possible heating effects, the current in the coil was turned off for ~ 5 min after every 10 min of AC B-field stimulation. The magnetic field at the center of the coil was measured using a Gauss meter (Magsys Magnetometer).

https://dx.doi.org/10.1021/acssensors.0c00664
ACS Sens. 2021, 6, 340−347

Dark-Field Microscopy. The dark-field microscopy (DFM) images were captured using an inverted optical microscope (Nikon Eclipse Ti−U) equipped with a dark-field condenser (Nikon, Ti-DF, NA ∼0.8−0.95) and a 40× objective lens (Nikon CFI Super Plan Fluor ELWD, NA = 0.6). (See Figure S1 of Supporting Information (SI).) A CCD camera (Point Gray Grasshopper 3) was used to capture the dark-field images. 100 μL of the NPs suspension in 10 mM PBS was placed at the liquid cell. The liquid cell was kept at the center of the solenoid. The nanopipette tip was placed horizontally within the liquid cell, and the motion of the MENPs was monitored with and without an AC B-field. As a control experiment, the DF video of the ∼50 nm MNP is also recorded.

Data Analysis. The experimental data was analyzed using OriginPro 2018, ImageJ, and custom-written LabVIEW programs. A moving average smoothing method with a 2 ms time window was typically applied to the current and potential results. The dV/dt time traces were smoothed by the moving average method using a 10 ms time window if not mentioned otherwise.

RESULTS AND DISCUSSION

MENP and Setup to Detect Single-MENP by a Nanopore-CNE Nanopipette. The transmission electron microscope (TEM) image of MENP is shown in Figure 1a. The MENP has irregular sphere-like morphology with an average size of 25 ± 5 nm. The XRD analysis of the MENP further confirms that MENPs are crystalline and composed of CFO and BTO.[5,13] For each MENP, the magnetostrictive CFO core is surrounded by a piezoelectric BTO shell. The mean zeta potential of MENPs was estimated to be −23.5 ± 5.8 mV using dynamic light scattering (DLS) based zeta potential measurements in 10 mM PBS (pH 7.1) solution. It has been reported that the zeta potential of MENP becomes more negative after applying a DC B-field.[4,13] When the magnitude of the B-field increases to 100 Oe, up to 30% increase in the zeta potential was observed. For comparison, the larger (∼50−100 nm size) MNP has a smaller mean zeta potential of about −15.4 ± 4.6 mV.

Figure 1b illustrates the mechanism of the detected surface charge increase of the MENP stimulated by an AC B-field. Under an AC B-field, a directional strain (ε) is produced in the magnetostrictive CFO core and transferred to the BTO shell as the mechanical stress. The mechanical stress leads to the charge redistribution on the piezoelectric BTO shell and the generation of additional net charges.

The general relationship between the applied strain (ε) and the generated electric potential (V) of piezoelectric material (e.g., BTO) is given as

$$\varepsilon = d \times V/\mathrm{l} \quad (1)$$

where d is the magnetoelectric coefficient and l is the thickness of the material. Assuming that CFO (core) and BTO (shell) have no gap at the interface and the strain generated along the same direction of the applied B field (60 Oe), the induced electric potential on the BTO shell of ∼6 nm thickness is estimated to be ∼−1.30 mV (see section S2). Here, we are interested in detecting the surface charge increase of the individual MENPs under an AC B-field.

The schematic of the experimental setup is illustrated in Figure 1c. The nanopore−CNE nanopipette utilized during this research has a long-taper geometry with pore diameter ranging from 50 to 90 nm. The average effective surface area of CNE is estimated to be 0.21 μm^2. All the experiments were conducted using eight well-characterized nanopipettes (P1−P8, see section S3). A constant bias V_{pore} is applied through the nanopore barrel. Before adding MENPs in the bath solution, both the current−time ($i-t$) and potential−time ($V-t$) traces acquired respectively through the nanopore and CNE were stable and featureless. After adding MENPs, small i and V changes appeared in the time traces. These transient changes are due to the interactions between NPs and the nanopipette apex, and most are at a single-NP level.[40] As illustrated in Figure 1d, two types of NP−nanopipette interaction events may be observed: (i) translocation through the nanopore and (ii) collision near the CNE surface.

Detection of AC B-Field Induced Surface Potential Change by MENP-CNE Collision Events. To understand the detected signals, let us first discuss the motion of the NPs in solution under various forces. In our experiment, the NP may experience 3 types of forces. First, the electric forces: the electric forces include the driving force by the applied positive nanopore bias and the repulsive electrostatic force by the negative surface charges of both glass and NPs. The estimated force induced by V_{pore} of 0.4 V is ∼100 pN (see section S4). Second, the Stokes drag force results from the viscosity of the solution and is on the order of 0.001 pN (see SI4). Third, the magnetic force due to the external B-field: since the magnetic field is uniform at the center of the solenoid, magnetic NPs do not experience magnetic force, but only magnetic torque. Therefore, the B-field only induces the rotational motion but not the translational motion of the magnetic NPs. The estimated magnitudes of angular velocity and the corresponding tangential linear velocity of MENP at 60 Oe AC B-field are 433 rad/s and 6.5 μm/s, respectively (see SI4). For comparison, the corresponding values for MNP are 1032 rad/s and 25.5 μm/s.

We imaged the movement of individual MENPs in solution by DFM under the same experimental conditions. No visible differences can be noticed from the MENPs' motion with and without the AC B-field (see Video S1a). The MENPs maintained their random motions and did not oscillate with the applied AC frequency (various frequencies have been tested), confirming that no magnetic force is applied on the MENPs. It is also the same for MNPs (see Video S1b).

The simultaneous measurements of current and potential via the nanopore and CNE can help to separate types (i) and (ii) events. A typical NP-CNE collision event induces obvious changes of V of the CNE but a negligible change of i of the nanopore. However, the NP translocation events through the nanopore produce obvious and correlated i and V changes. Based on the observed current and potential changes, translocation events of MENPs through the nanopore only happen occasionally both with and without the AC B-field (see Figure S2). The low translocation event rate is attributed to the high entrance barrier of nanopore for MENPs. The entrance barrier arises from the surface charge of the quartz surface and the entropy penalty. In contrast, we detected a large number of collision events from the CNE. It should be noted that the NPs do not need to physically touch the CNE surface to be detected in the NP-CNE collision events. Most events are actually detected when the NP double layer and the CNE sensing zone overlap. This is reflected from the facts (see below) that most of the detected surface potentials are much smaller than the zeta potential of NP. With a larger detection distance range, more collision events are observed. Below, we will focus on the type (ii) NP-CNE collision events.

Figure 2a (i) shows a typical $V-t$ trace (red color) with continuous potential changes when no AC B-field is applied. More data is shown in Figure S3a. This data was collected by

https://dx.doi.org/10.1021/acssensors.0c00664
ACS Sens. 2021, 6, 340−347

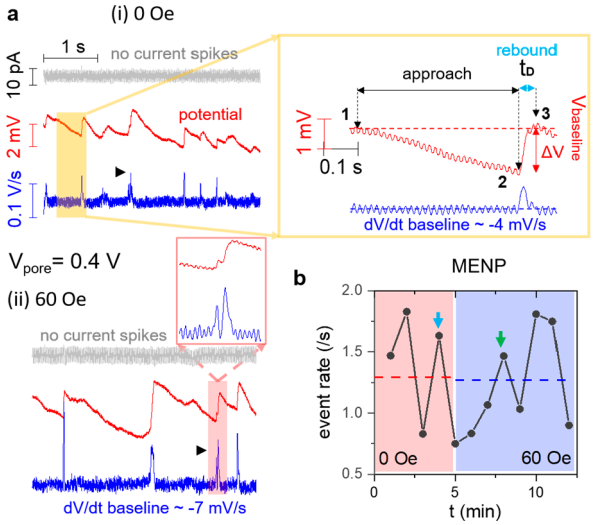

Figure 2. (a) Typical time traces of current (gray), potential (red), and the first derivative of potential (blue) at V_{pore} = 0.4 V (i) without and (ii) with an AC B-field. The zoomed image of a potential dip illustrating the collision event in 2 steps, approach (1−2) and rebound (2−3). ΔV denotes the amplitude of the potential dip. The t_D is the time duration of the rebounding. The black arrows and zoomed image of a potential dip in (ii) denote a collision event due to two clustered MENPs. (b) MENP collision event rate as a function of time without (light red region) and with (light blue region) a 60 Oe AC B-field stimulation. Each point is averaged over 1 min data. The blue and green arrows denote the time at which time traces (i) and (ii) are recorded, respectively.

nanopipette P1 at V_{pore} = 0.4 V. There are no corresponding current changes in the current trace (gray color). Therefore, these potential changes are induced by MENP-CNE collision events. The shape of the potential dips suggests that most of them are single-NP events. The small clustered NPs often generate a staircase increase in the rebounding section of the potential dip and multiple peaks in the dV/dt trace. Two such events are indicated by the black arrows in Figure 2a (i) and (ii) traces, with more examples shown in Figure S3b. The right side of Figure 2a (i) shows the zoomed image of a potential dip from a single-NP event. The general feature of these reveals the approach (points 1 to 2) and rebounding (points 2 to 3) motions during a MENP-CNE collision event. Based on the dV/dt magnitude (the blue color trace), the speed of approach is significantly slower than the speed of rebounding. When an AC B-field is applied (see Figure 2a (iii)), the magnitude ΔV of a large fraction of potential dips increases obviously. Correspondingly, both the approaching and rebounding dV/dt magnitudes of these potential dips are increased obviously. We believe the observed increases are due to the increased surface charge of MENPs under an AC B-field stimulation.[2,4,7]

To confirm, we performed control experiments using MNP at the same experimental conditions. As shown in Figure S3c of Supporting Information, the observed potential dips induced by the single MNP-CNE collision event show similar shapes at V_{pore} = 0.4 V with zero or 60 Oe AC B-field. No obvious difference is noticed in the ΔV and dV/dt magnitudes of the potential dips when the B-field is changed from 0 to 60 Oe. The insensitivity to the AC B-field stimulation is expected because the MNPs lack the magneto-electric property.

Figure 2b shows the event rate of potential dips as a function of time for MENPs with 0 and 60 Oe AC B-field. At both B-fields, the event rate varies between ∼0.5 and ∼2 events/s with an average value of ∼1.2 events/s over 5 min. The fluctuations of the event rate reveal the dynamic changes of MENP local concentration near the CNE, which are induced by the dynamic accumulations and dispersion of NPs near the apex. In the control experiments with MNPs, the event rate as a function of time without/with an AC B-field are presented in Figure S4. The average event rate is ∼0.24 events/s.

Based on the Stokes−Einstein relationship using bulk concentration, we estimate that diffusion-limited event rates

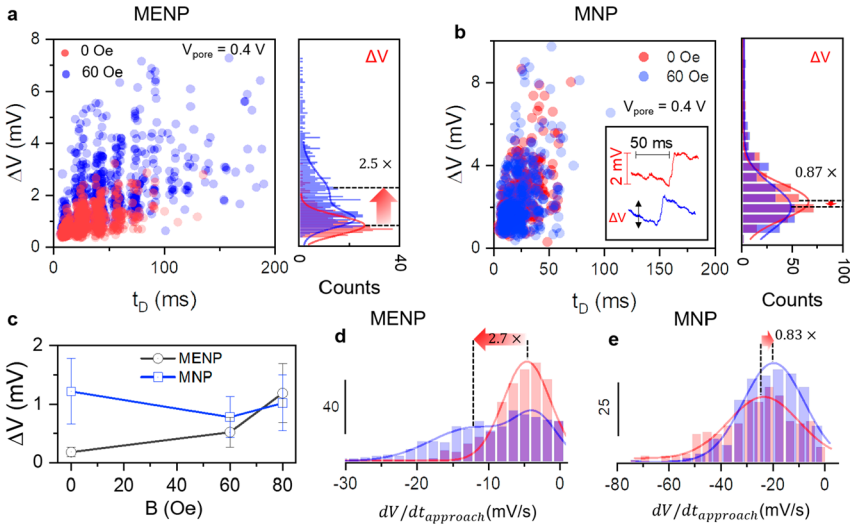

Figure 3. Statistics of collision events of MENP and MNP detected by the nanopipette at V_{pore} = 0.4 V. (a) Scatter plot of ΔV−t for the MENP-CNE collision events without (blue, N = 427) and with (red, N = 628) the AC B-field using nanopipette P1. The histograms at the right side show potential dip amplitude (ΔV). (b) Scatter plot of ΔV−t for the MNP-CNE collision events without (N = 316) and with (N = 302) the AC B-field using a nanopipette P2. The histograms at the right show potential dip amplitude (ΔV). The inset denotes the typical nanoimpact events without (i) and with (ii) an AC B-field. (c) ΔV vs AC B-field intensity plot for the MENP and MNP using nanopipettes P3 and P4, respectively. The y-error bars are the standard deviation from the mean value. The distributions of dV/d$t_{approach}$ of the MENP-CNE (d) and MNP-CNE (e) collision events at zero (red color) and 60 Oe (blue color) AC B-field. Solid lines in the histograms are Gaussian fits.

https://dx.doi.org/10.1021/acssensors.0c00664
ACS Sens. 2021, 6, 340−347

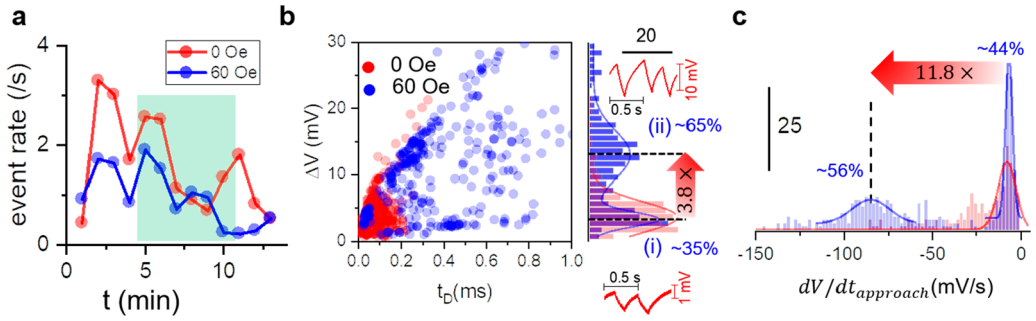

Figure 4. Statistics of MENP-CNE collision events from the surface modified nanopipette P7 without (red) and with (blue) AC B-field stimulation. (a) MENP-CNE collision event rates as a function of time. The events in the shaded regions are used for analysis. (b) Scatter plot of ΔV vs t_D for the MENP-CNE collision events. The histograms on the right side show the potential amplitude distributions. The potential time trace in the inset of histogram presents the type (i) and type (ii) events appeared in the ΔV histogram distribution. (c) Potential slope analysis of the MENP-CNE collision events without/with AC B-field. Solid lines in the histograms are Gaussian fits.

are 8.45 events/s and 1.26 events/s for MENP and MNP, respectively (see section S8). The smaller theoretical event rate of MNP is due to its larger size. For MENP, the theoretical value is about 18 times higher than the experimental value (0.46/s) at zero V_{pore}. Similarly, for MNP, the theoretical value is ~6 times higher than the experimental value (0.21/s) at zero V_{pore}. One possible reason for the lower experimental value is the smaller actual bulk concentration of NP considering the loss of NPs due to surface adsorption and aggregation. Between MENP and MNP, the MENPs are less stable at the zero B-field. However, the stimulation of AC B-field can effectively improve the stability of the MENPs, which is attributed to their increased surface charge and the rotation motion. Another possible reason for the lower event rate in experiments is attributed to the electrostatic repulsion between negatively charged NPs and the nanopipette apex, which prevents some NPs from moving closer to the CNE. We noticed that the event rate is typically higher at 0.4 V than at 0 V. The applied positive V_{pore} helps to compete with the repulsive force, thus boosting the event rate. For MENP, the V_{pore}-dependent event rate increase is more obvious under a stronger B-field. Therefore, the B-field induced surface change enhancement amplifies the V_{pore} effect.

Statistical analysis results of the potential dips without/with AC B-field for MENP are presented in Figure 3a. Only potential dips that are clearly separated and less affected by the adjoining MENPs were analyzed. The ΔV vs t_D scatter plots and the corresponding ΔV histograms of the MENP potential dips at zero and 60 Oe AC B-field are shown in Figure 3a. In the scatter plots, the distribution of data with 60 Oe AC B-field (blue color) is much broader with more points showing bigger ΔV and t_D. At zero B-field, the red color ΔV histogram shows one peak with the mean ΔV ~0.77 ± 0.37 mV. At 60 Oe B-field, a shoulder peak appears near the main peak in the blue color ΔV histogram. The width of the shoulder peak is broader and with contributions from about 45% of the total events. The main peak of the blue color histogram is very close to the peak of the red color histogram. However, the two-peak Gaussian fit to the histogram gives a mean ΔV ~ 1.95 ± 0.79 mV for the shoulder peak. It is an increase of ~2.5 times in magnitude from −0.77 mV to −1.95 mV. The broad distribution likely reflects the heterogeneous response of the MENPs to the stimulation of the AC B-field.[4] Previous study showed that the surface charge enhancement is proportional to the strain deformation of the BTO shell.[4] The structural heterogeneity between MENPs, such as size, shape, and surface curvature variations, may produce different surface charge increase on the MENPs-shell surface.

For comparison, the statistical analysis results of the potential dips of control experiment MNPs are shown in Figure 3b. The distributions of data points in the ΔV vs t_D scatter plots are similar at both zero and 60 Oe AC B-field. Both ΔV histograms only show one peak, which can be fitted by the one peak Gaussian function. The mean ΔV values are 2.07 ± 0.86 mV at 0 Oe and 1.80 ± 1.08 mV at 60 Oe, respectively. The ΔV of MNPs with 60 Oe AC B-field is slightly smaller than with zero AC B-field. This is contrary to the results of MENPs in Figure 3a.

Previous DLS measurements have shown that with the increase of the applied DC B-field strength, the zeta potential of the MENPs increases.[13] We further checked the ΔV change at 80 Oe B-field. The plot in Figure 3c shows the ΔV of MENP increases with the increase of the AC B-field amplitude. The mean ΔV values of the shoulder peak at 60 and 80 Oe are used in the plot. The overall trend of the charge enhancement is similar to the previous report. In contrast, the ΔV of MNPs does not show the increasing trend with the increase of the AC B-field (blue color) (see also Figure S5).

The MENP results in Figure 3 are acquired at V_{pore} = 0.4 V. At zero V_{pore} bias, the ΔV of the potential dip is smaller. When the V_{pore} is increased from zero to 400 mV, the ΔV increases by 13% at 0 Oe but by 34% at 60 Oe B-field (see Figure S6). The V_{pore} induced ΔV increase is bigger with the AC B-field, which also originated from the B-field induced surface charge enhancement of MENPs. The same V_{pore} can produce a bigger electric force on the approaching MENP with the increased surface charge, leading to a smaller MENP-CNE distance during the collision and thus an increased ΔV in the potential dip.

We further compared the mean approach slope ($dV/dt_{approach}$) of potential dips for MENPs at 0.4 V with and without a 60 Oe B field. The distribution of $dV/dt_{approach}$ is shown in Figure 3d. The mean $dV/dt_{approach}$ at 0 and 60 Oe AC B-field are ~−4.3 ± 3.2 mV/s and ~−11.7 ± 6.1 mV/s, respectively. The dV/dt value is ~2.7 times larger when the AC B-field is increased from 0 to 60 Oe. The increase of $dV/dt_{approach}$ suggests the increase of the approaching speed of the MENP, which is induced by the increased electric force on the MENP with the AC B-field. In contrast, in the MNP control experiment, the $dV/dt_{approach}$ value is slightly reduced by ~13% with the 60 Oe AC B-field (Figure 3e). MNPs slow down slightly as they approach the CNE in the presence of the AC B-

https://dx.doi.org/10.1021/acssensors.0c00664
ACS Sens. 2021, 6, 340−347

field. This observation is consistent with the slightly reduced ΔV for the MNP in the presence of AC B-field. The small change may be attributed to the rotational motion of the MNP in a B-field.

Between MENPs and MNPs, the mean ΔV and $dV/dt_{approach}$ are both bigger for MNPs under the same 60 Oe AC B-field and 0.4 V V_{pore} bias. Because the motion of NP is mainly driven by the electric forces instead of diffusion, the differences can be attributed to the bigger size of MNP, which induced a bigger floating potential change at the CNE when both the NP-CNE distance and CNE size are the same. In addition, the smaller electrostatic repulsion experienced by the MNP (smaller zeta potential) also helps the MNP be closer to the CNE with a bigger approaching speed.

Changes of Potential Dips of MENP-CNE Collision Events by Modified Nanopipette. The high negative surface charge of the nanopipette apex slowed down the approaching motion of MENP and prevented it from getting closer to the CNE surface. To suppress the surface charge effect, we also chemically modified the quartz surface with a neutral molecule (see method). Indeed, the average event rate increased by 32% after the chemical modification in both cases (Figure 4a) using the nanopipette with very similar characteristics as before. Figure 4b shows the statistical analysis of the potential dips at V_{pore} = 0.4 V and with 0 or 60 Oe AC B-field. More data can be found in Figure S7. Before applying the AC B-field, the potential distribution is a single peak with the mean value ΔV of ~3.35 ± 2.30 mV. With the 60 Oe AC B-field, the ΔV distribution is much broader and bimodal, with two average ΔV values at ~3.10 ± 1.10 mV and ~12.90 ± 3.65 mV. The value of the first ΔV is close to the one measured without AC B-field. After surface modification, the overall increase in the detected MENPs surface potential in the absence of an AC B-field is expected as the electrostatic repulsion is weaker between the MENPs and the nanopipette apex. Stimulated by 60 Oe AC B-field, the ΔV is increased by ~3.8 times.

We further analyzed the approach slope of the potential dip to derive the approaching speed of the MENP toward the CNE (Figure 4c). The average value of the slope is −7.2 ± 5.1 mV/s without the AC B-field stimulation. With the AC B-field, we detected two values −6.1 ± 4.2 mV/s and −84.6 ± 11.2 mV/s. The first one is also attributed to the MENPs without surface charge increase. The latter one is about 11.8 times higher than the measured value without the presence of the AC B-field. Therefore, compared with the data of nonmodified nanopipette, the data using a modified nanopipette reveal the same trend of change triggered by the applied AC B-field. However, the increase of both ΔV and dV/dt of the potential dip signals is more obvious and bigger. The difference is attributed to the smaller electrostatic repulsion by the nanopipette surface charge. Therefore, the NPs can be closer to the CNE. These bigger changes better illustrate the surface charge/potential increase of MENP under the stimulation of AC B-field.

CONCLUSION

The AC B-field stimulated surface charge enhancement of MENPs was carefully examined at the single-NP level in this research by probing the OCP change of a floating nanoelectrode during the "nanoimpact" events by individual MENPs. By analyzing the motion pattern of individual NPs during the collision events before and after the application of an AC B-field, we can confirm the surface charge/potential enhancement of MENPs stimulated by the AC B-field. This study also suggests that in applying AC B-field stimulation, the surface potential increase in nanoparticle surface potential change is due to the presence of the piezoelectric shell of MENP. The proposed scientific reasoning was validated using a positive control of MNP wherein piezoelectric shell is absent. We also noticed the obvious heterogeneity in the response to the B-field stimulation, which may provide a convenient way to evaluate the uniformity of the synthesized MENP, the effects of MENP size, and surface curvature to the AC B-field stimulation or the aging of MENP with time.

The results of "nanoimpact"-based single-MENP analysis method have confirmed the effective remote tuning of the surface potential of MENP by the applied AC B-field. In the next step, we will use the same method to probe the magneto-elastic wave produced by the MENPs upon the stimulation of the AC B-field. The MENPs with tunable magneto-elasto-electric properties should have immediate biomedical applications. MENPs-supported therapies have the potential to be the most efficient nanoparticle-based therapies where targeted drug delivery, image-guided therapy, on-demand controlled release, and stimuli responsiveness-based treatments are the key requirements.[16,44,45] Such therapies can be the possible new treatment for central nervous system (CNS) diseases, cancer, brain stimulation, etc., even in a personalized manner.

We also demonstrated the capability of the potentiometric single-entity "nanoimpact" technique. Most of the current "nanoimpact" methods relied on the electrochemical current signal. If the NP is not redox-active, additional redox mediators are needed in the solution. The colliding NP also needs to be in the tunneling distance with the ultrasmall electrode surface to be detected. In contrast, no electron transfer process is needed for the OCP based measurement. The NP can be detected over a much larger distance. The single-NP OCP signal is also easy to be measured by the amplifier in the low gain and high bandwidth settings, allowing for higher sensitivity and faster detection. Therefore, the potentiometric single-entity "nanoimpact" technique is suitable to detect non-electroactive biomolecules, such as nucleic acids and proteins, without adding redox mediators in the solution.

ASSOCIATED CONTENT

Supporting Information

The Supporting Information is available free of charge at https://pubs.acs.org/doi/10.1021/acssensors.0c00664.

Nanopipette characterization, additional experimental data of NP-CNE collision events, and nanopore translocation events, theoretical estimations of forces, and torque on NPs (PDF)

DF video of MENP with and without AC B-field (MP4)

DF video of MNP with and without AC B-field (MP4)

AUTHOR INFORMATION

Corresponding Authors

Jin He − *Physics Department and Biomolecular Science Institute, Florida International University, Miami, Florida 33199, United States;* orcid.org/0000-0002-2633-9809; Email: jinhe@fiu.edu

Ajeet Kaushik − *NanoBioTech Laboratory, Department of Natural Sciences, Division of Sciences, Art, & Mathematics, Florida Polytechnic University, Lakeland, Florida 33805,*

https://dx.doi.org/10.1021/acssensors.0c00664
ACS Sens. 2021, 6, 340−347

United States; orcid.org/0000-0003-4206-1541; Email: akaushik@floridapoly.edu

Authors

Popular Pandey − *Physics Department, Florida International University, Miami, Florida 33199, United States;* orcid.org/0000-0002-1899-3480

Govinda Ghimire − *Physics Department, Florida International University, Miami, Florida 33199, United States*

Javier Garcia − *Physics Department, Florida International University, Miami, Florida 33199, United States*

Alberto Rubfiaro − *Physics Department, Florida International University, Miami, Florida 33199, United States*

Xuewen Wang − *Physics Department, Florida International University, Miami, Florida 33199, United States;* orcid.org/0000-0002-5323-8309

Asahi Tomitaka − *Department of Immunology and Nanomedicine, Institute of Neuroimmune Pharmacology, Herbert Wertheim College of Medicine, Florida International University, Miami, Florida 33199, United States*

Madhavan Nair − *Department of Immunology and Nanomedicine, Institute of Neuroimmune Pharmacology, Herbert Wertheim College of Medicine, Florida International University, Miami, Florida 33199, United States*

Complete contact information is available at: https://pubs.acs.org/10.1021/acssensors.0c00664

Notes

The authors declare no competing financial interest.

■ ACKNOWLEDGMENTS

This work was supported by the Engineering Research Centre Program of the National Science Foundation under NSF Cooperative Agreement No. EEC-1647837 and NSF CBET 1454544. P.P. would like to thank the University Graduate School at Florida International University for providing the Dissertation Year Fellowship. This work is dedicated to the memory of Professor Nongjian Tao.

■ REFERENCES

(1) Karimi, M.; Ghasemi, A.; Sahandi Zangabad, P.; Rahighi, R.; Moosavi Basri, S. M.; Mirshekari, H.; Amiri, M.; Shafaei Pishabad, Z.; Aslani, A.; Bozorgomid, M.; Ghosh, D.; Beyzavi, A.; Vaseghi, A.; Aref, A. R.; Haghani, L.; Bahrami, S.; Hamblin, M. R. Smart micro/nanoparticles in stimulus-responsive drug/gene delivery systems. *Chem. Soc. Rev.* **2016**, *45* (5), 1457−1501.

(2) Hu, J.-M.; Eom, C.-B. Magnetic-field control of ionic bonds on ferroelectric surfaces. *Appl. Phys. Lett.* **2019**, *114* (9), No. 091601.

(3) Stimphil, E.; Nagesetti, A.; Guduru, R.; Stewart, T.; Rodzinski, A.; Liang, P.; Khizroev, S. Physics considerations in targeted anticancer drug delivery by magnetoelectric nanoparticles. *Appl. Phys. Rev.* **2017**, *4* (2), No. 021101.

(4) Betal, S.; Shrestha, B.; Dutta, M.; Cotica, L. F.; Khachatryan, E.; Nash, K.; Tang, L.; Bhalla, A. S.; Guo, R. Magneto-elasto-electroporation (MEEP): In-vitro visualization and numerical characteristics. *Sci. Rep.* **2016**, *6*, 32019.

(5) Kaushik, A.; Nikkhah-Moshaie, R.; Sinha, R.; Bhardwaj, V.; Atluri, V.; Jayant, R. D.; Yndart, A.; Kateb, B.; Pala, N.; Nair, M. Investigation of ac-magnetic field stimulated nanoelectroporation of magneto-electric nano-drug-carrier inside CNS cells. *Sci. Rep.* **2017**, *7*, 45663.

(6) Betal, S.; Dutta, M.; Cotica, L. F.; Bhalla, A.; Guo, R. BaTiO3 Coated CoFe2O4−Core-Shell Magnetoelectric Nanoparticles (CSMEN) Characterization. *Integr. Ferroelectr.* **2015**, *166* (1), 225−231.

(7) Sablik, M. J.; Telschow, K. L.; Augustyniak, B.; Grubba, J.; Chmielewski, M. Relationship between magnetostriction and the magnetostrictive coupling coefficient for magnetostrictive generation of elastic waves. *AIP Conf. Proc.* **2001**, *615* (1), 1613−1620.

(8) Ma, J.; Hu, J.; Li, Z.; Nan, C.-W. Recent Progress in Multiferroic Magnetoelectric Composites: from Bulk to Thin Films. *Adv. Mater.* **2011**, *23* (9), 1062−1087.

(9) Wang, Y.; Hu, J.; Lin, Y.; Nan, C.-W. Multiferroic magnetoelectric composite nanostructures. *NPG Asia Mater.* **2010**, *2*, 61.

(10) Tang, X.; Kou, L. Two-Dimensional Ferroics and Multiferroics: Platforms for New Physics and Applications. *J. Phys. Chem. Lett.* **2019**, *10* (21), 6634−6649.

(11) Domann, J.; Wu, T.; Chung, T.-K.; Carman, G. Strain-mediated magnetoelectric storage, transmission, and processing: Putting the squeeze on data. *MRS Bull.* **2018**, *43* (11), 848−853.

(12) Palneedi, H.; Annapureddy, V.; Priya, S.; Ryu, J. Status and Perspectives of Multiferroic Magnetoelectric Composite Materials and Applications. *Actuators* **2016**, *5* (1), 9.

(13) Rodzinski, A.; Guduru, R.; Liang, P.; Hadjikhani, A.; Stewart, T.; Stimphil, E.; Runowicz, C.; Cote, R.; Altman, N.; Datar, R.; Khizroev, S. Targeted and controlled anticancer drug delivery and release with magnetoelectric nanoparticles. *Sci. Rep.* **2016**, *6*, 20867.

(14) Kaushik, A.; Yndart, A.; Atluri, V.; Tiwari, S.; Tomitaka, A.; Gupta, P.; Jayant, R. D.; Alvarez-Carbonell, D.; Khalili, K.; Nair, M. Magnetically guided non-invasive CRISPR-Cas9/gRNA delivery across blood-brain barrier to eradicate latent HIV-1 infection. *Sci. Rep.* **2019**, *9* (1), 3928.

(15) Rodriguez, M.; Kaushik, A.; Lapierre, J.; Dever, S. M.; El-Hage, N.; Nair, M. Electro-Magnetic Nano-Particle Bound Beclin1 siRNA Crosses the Blood−Brain Barrier to Attenuate the Inflammatory Effects of HIV-1 Infection in Vitro. *Journal of Neuroimmune Pharmacology* **2017**, *12* (1), 120−132.

(16) Nair, M.; Guduru, R.; Liang, P.; Hong, J.; Sagar, V.; Khizroev, S. Externally controlled on-demand release of anti-HIV drug using magneto-electric nanoparticles as carriers. *Nat. Commun.* **2013**, *4* (1), 1707.

(17) Cuesta, A. Measurement of the Surface Charge Density of Co-Saturated Pt (111) Electrodes as a Function of Potential: The Potential of Zero Charge of Pt (111). *Surf. Sci.* **2004**, *572*, 11.

(18) Hirsch, V.; Kinnear, C.; Moniatte, M.; Rothen-Rutishauser, B.; Clift, M. J. D.; Fink, A. Surface Charge of Polymer Coated Spions Influences the Serum Protein Adsorption, Colloidal Stability and Subsequent Cell Interaction. *Nanoscale* **2013**, *5*, 3723.

(19) Tufenkji, N.; Elimelech, M. Breakdown of Colloid Filtration Theory: Role of the Secondary Energy Minimum and Surface Charge Heterogeneities. *Langmuir* **2005**, *21*, 841.

(20) Ohshima, H.; Healy, T. W.; White, L. R. Accurate Analytic Expressions for the Surface Charge Density/Surface Potential Relationship and Double-Layer Potential Distribution for a Spherical Colloidal Particle. *J. Colloid Interface Sci.* **1982**, *90*, 17.

(21) Chan, D. Y.; Pashley, R. M.; White, L. R. A Simple Algorithm for the Calculation of the Electrostatic Repulsion between Identical Charged Surfaces in Electrolyte. *J. Colloid Interface Sci.* **1980**, *77*, 283.

(22) Lin, N. H.; Shih, W. Y.; Lyster, E.; Cohen, Y. Crystallization of calcium sulfate on polymeric surfaces. *J. Colloid Interface Sci.* **2011**, *356* (2), 790−7.

(23) Bodhak, S.; Bose, S.; Bandyopadhyay, A. Role of Surface Charge and Wettability on Early Stage Mineralization and Bone Cell−Materials Interactions of Polarized Hydroxyapatite. *Acta Biomater.* **2009**, *5*, 2178.

(24) Sahın, Ö.; Nusret Bulutcu, A. Effect of Surface Charge Distribution on the Crystal Growth of Sodium Perborate Tetrahydrate. *J. Cryst. Growth* **2002**, *241*, 471.

(25) Manzini, M. C.; Perez, K. R.; Riske, K. A.; Bozelli, J. C.; Santos, T. L.; da Silva, M. A.; Saraiva, G. K. V.; Politi, M. J.; Valente, A. P.; Almeida, F. C. L. Peptide:Lipid Ratio and Membrane Surface Charge Determine the Mechanism of Action of the Antimicrobial Peptide Bp100. Conformational and Functional Studies. *Biochim. Biophys. Acta, Biomembr.* **2014**, *1838*, 1985.

(26) Bakhti, M.; Snaidero, N.; Schneider, D.; Aggarwal, S.; Möbius, W.; Janshoff, A.; Eckhardt, M.; Nave, K. A.; Simons, M. Loss of Electrostatic Cell-Surface Repulsion Mediates Myelin Membrane Adhesion and Compaction in the Central Nervous System. *Proc. Natl. Acad. Sci. U. S. A.* **2013**, *110*, 3143.
(27) Xiao, K.; Li, Y.; Luo, J.; Lee, J. S.; Xiao, W.; Gonik, A. M.; Agarwal, R. G.; Lam, K. S. The Effect of Surface Charge on in Vivo Biodistribution of Peg-Oligocholic Acid Based Micellar Nanoparticles. *Biomaterials* **2011**, *32*, 3435.
(28) Dobrovolskaia, M. A.; Patri, A. K.; Simak, J.; Hall, J. B.; Semberova, J.; De Paoli Lacerda, S. H.; McNeil, S. E. Nanoparticle Size and Surface Charge Determine Effects of Pamam Dendrimers on Human Platelets in Vitro. *Mol. Pharmaceutics* **2012**, *9*, 382.
(29) Chen, L.; McCrate, J. M.; Lee, J. C.; Li, H. The Role of Surface Charge on the Uptake and Biocompatibility of Hydroxyapatite Nanoparticles with Osteoblast Cells. *Nanotechnology* **2011**, *22*, 105708.
(30) Asati, A.; Santra, S.; Kaittanis, C.; Perez, J. M. Surface-Charge-Dependent Cell Localization and Cytotoxicity of Cerium Oxide Nanoparticles. *ACS Nano* **2010**, *4*, 5321.
(31) Ghosh, P. S.; Kim, C. K.; Han, G.; Forbes, N. S.; Rotello, V. M. Efficient Gene Delivery Vectors by Tuning the Surface Charge Density of Amino Acid-Functionalized Gold Nanoparticles. *ACS Nano* **2008**, *2*, 2213.
(32) Chung, T. H.; Wu, S. H.; Yao, M.; Lu, C. W.; Lin, Y. S.; Hung, Y.; Mou, C. Y.; Chen, Y. C.; Huang, D. M. The Effect of Surface Charge on the Uptake and Biological Function of Mesoporous Silica Nanoparticles in 3t3-L1 Cells and Human Mesenchymal Stem Cells. *Biomaterials* **2007**, *28*, 2959.
(33) Szekeres, M.; Tombácz, E. Surface Charge Characterization of Metal Oxides by Potentiometric Acid−Base Titration. *Colloids Surf., A* **2012**, *414*, 302.
(34) Gibson, G. T. T.; Mohamed, M. F.; Neverov, A. A.; Brown, R. S. Potentiometric Titration of Metal Ions in Ethanol. *Inorg. Chem.* **2006**, *45*, 7891.
(35) Sánchez, J.; del Valle, M. Determination of Anionic Surfactants Employing Potentiometric Sensors—a Review. *Crit. Rev. Anal. Chem.* **2005**, *35*, 15.
(36) Lu, S.-M.; Peng, Y.; Ying, Y.-L.; Long, Y.-T. Electrochemical Sensing at a Confined Space. *Anal. Chem.* **2020**, *92*, 5621.
(37) Baker, L. A. Perspective and Prospectus on Single-Entity Electrochemistry. *J. Am. Chem. Soc.* **2018**, *140* (46), 15549−15559.
(38) Wang, Y.; Shan, X.; Tao, N. Emerging tools for studying single entity electrochemistry. *Faraday Discuss.* **2016**, *193* (0), 9−39.
(39) Crooks, R. M. Concluding remarks: single entity electrochemistry one step at a time. *Faraday Discuss.* **2016**, *193* (0), 533−547.
(40) Pandey, P.; Panday, N.; Chang, S.; Pang, P.; Garcia, J.; Wang, X.; Fu, Q.; He, J. Probing Dynamic Events of Dielectric Nanoparticles by a Nanoelectrode-Nanopore Nanopipette. *ChemElectroChem* **2018**, *5* (20), 3102−3112.
(41) Pandey, P.; Garcia, J.; Guo, J.; Wang, X.; Yang, D.; He, J. Differentiation of metallic and dielectric nanoparticles in solution by single-nanoparticle collision events at the nanoelectrode. *Nanotechnology* **2020**, *31* (1), No. 015503.
(42) White, R. J.; Ervin, E. N.; Yang, T.; Chen, X.; Daniel, S.; Cremer, P. S.; White, H. S. Single Ion-Channel Recordings Using Glass Nanopore Membranes. *J. Am. Chem. Soc.* **2007**, *129* (38), 11766−11775.
(43) Panday, N.; Qian, G.; Wang, X.; Chang, S.; Pandey, P.; He, J. Simultaneous Ionic Current and Potential Detection of Nanoparticles by a Multifunctional Nanopipette. *ACS Nano* **2016**, *10* (12), 11237−11248.
(44) Guduru, R.; Liang, P.; Yousef, M.; Horstmyer, J.; Khizroev, S. Mapping the Brain's electric fields with Magnetoelectric nanoparticles. *Bioelectronic Medicine* **2018**, *4* (1), 10.
(45) Kaushik, A.; Rodriguez, J.; Rothen, D.; Bhardwaj, V.; Jayant, R. D.; Pattany, P.; Fuentes, B.; Chand, H.; Kolishetti, N.; El-Hage, N.; Khalili, K.; Kenyon, N. S.; Nair, M. MRI-Guided, Noninvasive Delivery of Magneto-Electric Drug Nanocarriers to the Brain in a Nonhuman Primate. *ACS Applied Bio Materials* **2019**, *2* (11), 4826−4836.

https://dx.doi.org/10.1021/acssensors.0c00664
ACS Sens. 2021, 6, 340−347